Maturity and Impedance Analysis of Organic-Rich Shales

Manika Prasad and **Kenechukwu C. Mba,** SPE; and **T. Elizabeth McEvoy** and **Michael L. Batzle,** SPE, Colorado School of Mines

Summary

Organic-rich shales (ORSs) need to be studied in detail to understand the provenance and the generation of hydrocarbons from source rocks. In recent years, ORSs have gained importance as hydrocarbon resources as well. Successful exploration and production programs for ORSs need reliable identification of their kerogen content as well as maturity through indirect seismic methods. However, the properties of kerogen are poorly understood, so predictions about maturity and rock-kerogen systems remain a challenge. Assessment of maturity from indirect measurements can be greatly enhanced by establishing and exploiting correlations between physical properties, microstructure, and kerogen content.

We show correlations between the impedance microstructure of ORSs and their maturity and elastic properties. We have used scanning acoustic microscopy to analyze and map the impedance microstructure in ORSs. We quantified textural properties in the images and related these textural properties to maturity and to impedance from acoustic-wave propagation measured at centimeter scales. This combined study of acoustic properties and microstructures of ORSs gives important insight into changes resulting from kerogen maturation. We introduce a modified porosity term and find that (1) there is a significant correlation between velocity and modified porosity of all ORSs; (2) imaging and quantifying microscale impedance texture and contrast in the images allow us to correlate them with ultrasonic measurements on a centimeter scale; and (3) textural heterogeneity, elastic impedance, velocity, and density increase with increasing shale maturity.

We also discuss possible methods to predict maturity from impedance on the basis of understanding the changes resulting from maturity in well-log response, core measurements, and microstructure of ORSs. Our work has important bearing on developing successful production and stimulation methodologies.

Introduction

ORSs and oil shales increasingly are being studied in detail to understand the provenance and the generation of hydrocarbon from source rocks. This recent interest stems from the recognition that ORSs are important self-contained hydrocarbon systems because they provide the source material and act as reservoir and seal formations. Because of our limited understanding of their hydrocarbon-generation and -storage capacity, it is challenging to assess reserves in ORS reservoir systems accurately. Furthermore, because shales are the most common sedimentary formation, reserves estimates of ORS reservoir systems have been updated dramatically in the past few years.

Successful exploration and production programs for ORSs must rely on an accurate identification of the kerogen content and its maturity through indirect seismic methods. The seismic properties of kerogen are poorly understood. Consequently, predictions of the seismic response of a rock/kerogen system and the kerogen maturity remain a big challenge. Kerogen maturity changes shale texture. For example, overpressure because of hydrocarbon generation can lead to microcracks and fractures in the matrix (Lempp et al. 1994). Assessment of maturity from indirect measurements can be enhanced greatly by exploiting any existing correlations between physical properties, microstructure, and kerogen content.

One way of looking at ORSs is through acoustic analysis. Numerous authors have shown that kerogen content, and with it maturity, can be related to *P*-wave velocity (Wert and Weller 1982; Mraz et al. 1983; Weller and Wert 1983; Passey et al. 1990; Vernik and Nur 1992; Vernik and Landis 1996; Vernik and Liu 1997; Prasad 2001; Prasad et al. 2002a). Velocity data measured in the laboratory by Vernik (Vernik and Nur 1992; Vernik and Landis 1996; Vernik and Liu 1997), hereinafter called the Vernik data set, show that V_p increases with increasing maturity except in high-porosity shales. In high-porosity (low-maturity) shales, V_p is better correlated with porosity. Within a single formation, the correlation between V_p and hydrogen index (HI) is reasonable, and the scatter is greatly reduced **(Fig. 1)** (Prasad et al. 2002a). In our study, we will examine the Bakken formation and investigate its acoustic and optical microstructure. We will also compare *P*- and *S*-wave velocities, V_p and V_s, respectively, measured in the laboratory, with sonic well-log data. The velocity measurements have led to our better understanding of the maturity processes in ORSs. By understanding the microstructures that lead to velocity variations with maturity, total organic content (TOC), and temperature, we can increase efficiency and reliability of fracture models and predict fracture placement better.

Description of Equipment and Samples Used

Our experimental techniques were based on the pulse transmission of acoustic waves through samples of known length. In one experiment, V_p and V_s were measured and the elastic moduli were derived from them. Sonic velocity data were also used from well logs from published sources. In the acoustic imaging experiment, we recorded the reflections of acoustic waves at each position on the sample in a raster described in detail in the following section.

Samples Used. We have used various ORS samples for our study. The Vernik data set belonged to the Bakken formation of the Williston basin in North Dakota, the Bazhenov formation in Western Siberia, the Woodford formation in Oklahoma, the Niobrara formation in New Mexico, the Monterey formation in California, and the Lockatong formation from New Jersey. The data (Vernik and Nur 1992; Vernik and Landis 1996, Vernik and Liu 1997) contain acoustic-pulse transmission-mode V_p and V_s data measured in three different directions, stiffness moduli for a transversely isotropic system, HI, volumetric kerogen content, porosity, and density. In the present study, we used the data measured on horizontal cores to investigate velocity correlations with other physical properties. We also used the anisotropic stiffnesses from the Vernik data set to study anisotropic effective-stress coefficients and to establish modulus-modified kerogen content-correlations.

We imaged a subset of the Vernik samples with scanning acoustic microscopy that allowed us to map impedance changes by scanning variations in reflected compressional waves across the samples. The acoustic imaging was made at high (GHz-range) and low (MHz-range) frequencies. We also measured V_p and V_s, and made acoustic scans on core samples from the Bakken formation of North Dakota.

Scanning Acoustic Microscopy. The acoustic images were made with a scanning acoustic microscope (SAM) at a frequency of

Copyright © 2011 Society of Petroleum Engineers

This paper (SPE 123531) was accepted for presentation at the SPE Rocky Mountain Petroleum Technology Conference, Denver, Colorado, USA, 14–16 April 2009, and revised for publication. Original manuscript received 23 July 2009. Revised manuscript received 13 February 2011. Paper peer approved 26 July 2011.

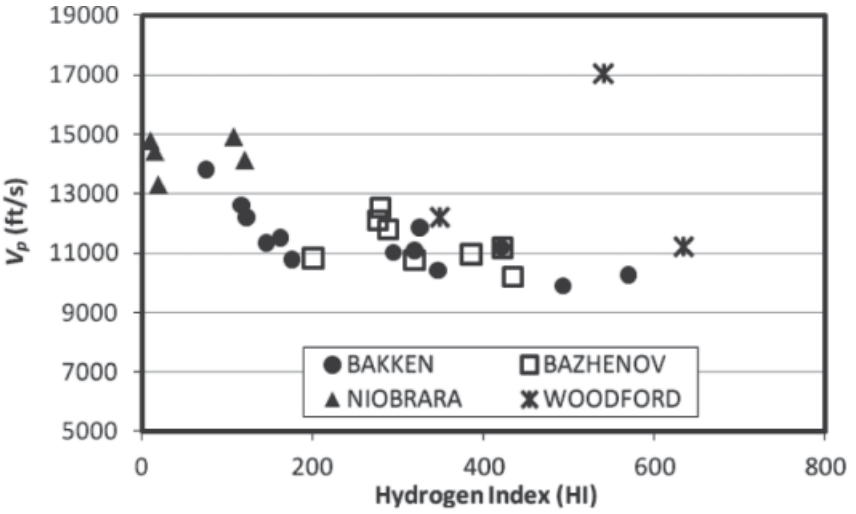

Fig. 1—*P*-wave velocity (V_p in ft/s) vs. HI. Lower HI corresponds to higher maturity. V_p is inversely proportional to HI and directly proportional to maturity. There is a marked increase in V_p as HI decreases below 200.

1 GHz to measure impedance in various rocks (for example, sandstones and shales). A complete description of the application of scanning acoustic microscopy to petrophysics can be found in Prasad (2001) and Prasad et al. (2002a). Here, we describe only main principles.

SAM can be best understood as microscopic analogs to side-scan sonar, zero-offset reflection seismic mapping, or ultrasound sonography. The main principle is to study surface and subsurface features with the help of high-frequency acoustic waves. Images of surface and subsurface microstructures are prepared on the basis of reflected acoustic waves that depend on the impedance changes in the sample. Acoustic waves that are incident on a sample are mode converted, partly transmitted into the sample, and partly reflected. The signal intensity received back at the transducer is governed by changes in acoustic impedance and hence by changes in the elastic constants of the material.

Three basic types of scans can be obtained from SAM:

1. An X-*t* scan (t = time), or an A-scan. This 1D A-scan is the primary information received at the transducer. An analog to reflection seismic would be a seismic line trace. The A-scan shows variations in signal amplitude with time received at a fixed lens position.

2. An X–Z scan, or a B-scan. In analogy to a reflection seismogram, recording several A-scans (seismic traces) along a line makes a B-scan. Any layering, alignment of grains and pores, of clusters of grains with the same impedance can be mapped by these vertical 2D scans.

3. An X–Y scan, or a C-scan. This is a horizontal 2D scan, similar to a side-scan sonar image. It is created by gathering information at a fixed time position on the A-scan and moving the lens in X- and Y-direction. Data obtained at time $t > 0$ gives the image of a subsurface layer.

SAM results of kerogen-rich shales were obtained with a high-frequency (0.2 to 2 GHz) and a low-frequency (10 to 50 MHz) acoustic microscope, both operating in reflection mode. The depth of penetration and resolution of microstructural features depend on the operating frequency. The 1-GHz high-frequency lens was used for high resolution of approximately 1 μm with a scan area of 1 × 1 mm. At frequencies in the GHz range, the opening angle of the acoustic lens is optimized to achieve a high sensitivity to surface acoustic (Rayleigh) waves. This design allowed us to map microstructural features from the interference patterns between normally reflected longitudinal waves and the Rayleigh waves (Briggs and Kolosov 1992). MHz-range low-frequency lenses were used for low resolution of approximately 30 μm with larger (cm-scale) scan areas. These scans allowed us to map large-scale microstructural features from the normally reflected longitudinal waves.

C-scans of surface and subsurface features can be used to study impedance changes in the sample quantitatively. By making a gray-scale calibration using materials of known impedance, the acoustic images of the rocks can be evaluated for impedance variations as functions of cementation strength, kerogen maturity, and reflectivity. To make a calibrated image, a set of standard materials is selected. The expected impedance in the unknown sample should lie within the impedance values of the standard materials. The standard samples are imaged at a fixed setting of signal and video gains such that all samples can be imaged at that setting. The gray scale of each sample image is associated with its independently measured impedance and its reflection coefficient with respect to the coupling medium, water. This gives rise to a calibration of the gray scale from 0 (= black) to 255 (= white). Next, the unknown sample is first imaged at an optimum gain setting. Then, the gain setting is reverted to the calibration values and an image is recorded. The gray-scale variations in the unknown image can then be determined from the calibration plot of reflection coefficient vs. impedance on the basis of a least-squares fit. Approximately 10 to 15% error is to be expected because of instrumental drift, especially if calibrations are not performed often or if the sample has large variations in surface topography. The calibration procedure and calibration samples are described in Prasad (2001) and Prasad et al. (2002a). In this study, only the high-frequency acoustic images were made with calibrated gray scales.

At low frequencies, depth information can be obtained by focusing the acoustic waves below the surface of the sample. The signals received back at the lens will then contain information about the entire path, from the surface to the focal point inside the sample. Such images are called defocussed images. **Fig. 2** shows a typical acoustic image of a USD 0.25 coin, with the surface image created from acoustic reflections in Fig. 2a. The corresponding defocussed image at a depth of 2 mm is displayed in Fig. 2b. The "tails" imprint of the coin is seen together with the surface information. Such images can be very useful to obtain information about any cracks, fractures, and subsurface inhomogeneities.

In this paper, we will show acoustic images of the Bakken formation obtained with GHz and MHz acoustic lenses. We will then relate them to acoustic measurements made on the samples at a centimeter scale. Because the microstructural information is also obtained from impedance contrasts, any changes in seismic velocities will be related to microstructural and compositional changes. In this manner, we explore causes for seismic velocity changes pertaining to maturity (Prasad et al. 2002a).

Pulse-Transmission Experiments. We also measured V_p and V_s at 1 MHz in a number of core plugs from the Bakken formation

(a) (b)

Fig. 2—Scanning acoustic image of a USD 0.25 coin: (a) shows a surface image and (b) was obtained by focussing approximately 2 mm (300 ns) into the coin.

at bench-top conditions, mainly to assess anisotropy and measure velocity difference with the well-log measurements to estimate possible core damage because of stress release and storage. We expect a maximum experimental error of 1% in the measurements, but a larger source of velocity discrepancy is the difference in pressure, frequency, and sample size in the laboratory. The core samples originate from depths greater than 7,000 ft. Pressure release can lead to microfracturing. Velocity dispersion can also lead to higher velocities measured in the laboratory at 1 MHz as compared with sonic log measurements at tens of kHz. These two effects compete against each other, and depending on the presence of compliant pores as well as attenuation, they can be fairly significant.

Presentation of Data and Results

We studied ORSs under an SAM to understand their microstructural properties and the causes for the elastic anisotropy. Acoustic microscopy allows us to map the impedance microstructure of samples using reflected acoustic waves. Three sets of samples were studied from various stages of kerogen maturation: diagenesis, catagenesis, and metagenesis. Microstructural and impedance differences are observed as the shales undergo the different stages of maturation. These changes can be related to the velocity anisotropy measured with ultrasonic-pulse-transmission methods.

Acoustic Images at MHz Frequencies. In the low-frequency (MHz) SAM system, the microstructural properties are studied from reflection of longitudinal waves at various interfaces in the sample. Normally reflected longitudinal waves contribute toward the impedance information on the sample. In the low-frequency acoustic images, two types of scans are obtained, a C-scan and a B-scan. The C-scan gives us a surface or subsurface image and the B-scan a zero-offset reflection profile. In analogy to reflection seismic mapping, reflections occur at interfaces where the waves encounter an impedance change. If this interface is continuous, it will be mapped as a layer in the B-scan. The layers can be mapped in 3D by combining multiple B-scans made at various locations on the sample and analyzed to map dips, subsurface cracks, and faults.

The acoustic scans obtained at 15 to 50 MHz and at 1 GHz gave important insight into the changes in texture with maturity and depth. Changes in maturity are expected to be accompanied by changes in microstructure such as those documented during hydrous pyrolysis experiments by Lewan (1987). Prasad et al. (2002a) calculated that the ultrasonic velocity increases by approximately 20% from Stage II maturity (HI = 584) to Stage IV maturity (HI = 122) in the Bakken, from the Vernik data set.

The shale samples used for V_{p0} measurements were coated with varnish to prevent them from swelling on contact with water. They were then used for acoustic scanning experiments at 15 MHz. Acoustic B- and A-scans of an immature Woodford shale sample (7,068 ft) are presented here in **Fig. 3,** and SAM C-scan images are shown in **Fig. 4.** The SAM C-scan images show representative impedance changes and can be used to understand the reflectivity patterns in the A-scans of Fig. 3. The impedance change between the coarse-grained layer (Fig. 4, right) and the fine-grained layer (Fig. 4, left) gives rise to a strong reflection (Fig. 3, right). This reflector is not observed in the A-scan of the same sample made by turning the sample 180° (Fig. 3, left). The contact between the two layers is closer to the top here. The event is masked by the high reflectivity of the shale.

A 3D reconstruction of the B-scans from each side **(Fig. 5)** demonstrates the continuity of the layers and the high reflectivity in the shale. Similar reconstruction of two Bakken shales (immature at 8,630 ft and mature at 11,246 ft) is shown in **Figs. 6 and 7,** respectively. Again, a similar pattern is observed. These patterns help explain the acoustic-velocity anisotropy measured in pulse-transmission experiments.

Fig. 8a shows a low-frequency focused image of a sample with sharp contrast between the Upper Bakken in the lower part of the image and the underlying Three Forks siltstone in the upper part of the image. The change in texture, along with the prevalence of microfractures in the upper part of the image, emphasizes the change across the contact. Fig. 8b is a zoomed-in image from the lower part of Fig. 8a showing the dark gray shades. This indicates lower impedances in the kerogen-rich shale. Fig. 8c is zoomed into the upper part of Fig. 8a and shows a lighter-gray, higher-impedance fractured zone above contact. **Fig. 9** shows samples with even finer-grained matrix in contrast with Fig. 8. These samples are below the resolution of the 50-MHz transducer. Future work is planned with higher-frequency tranducers to improve the impedance imaging of these samples.

Acoustic Images at 1 GHz. Despite similar chemical compositions, microstructure of the samples differed considerably. Acoustic micrographs of the Bakken shale series samples arranged in order of increasing maturity are shown in **Figs. 10 through 12.** These C-scan surface images were made at 1 GHz. All figures

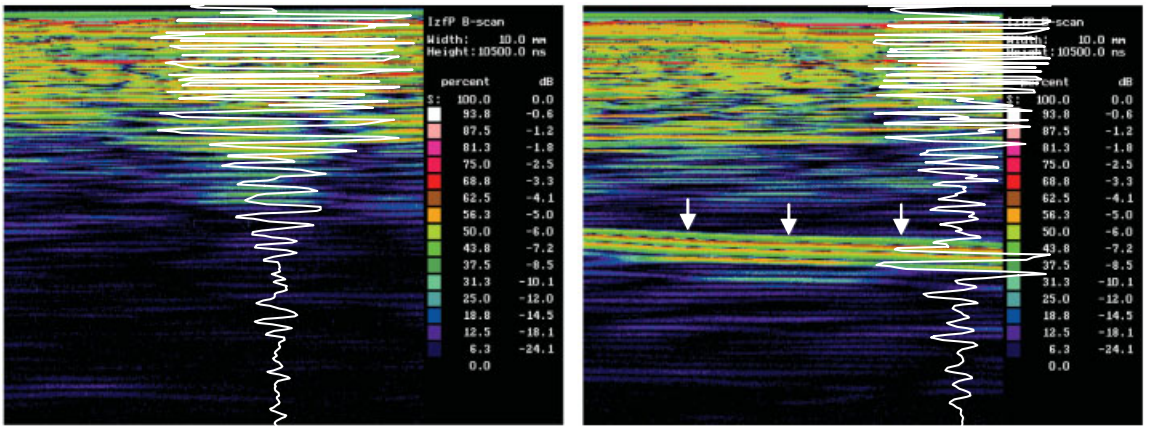

Fig. 3—Acoustic sounding of an immature Woodford shale (7,068 ft) at 15 MHz. Images are made of the same sample from opposite directions: The left image has the coarse-grained, high-impedance layer on top. The contact is at 5.5 mm (= 1.4 μs). Right image has the coarse grained, high impedance layer at the bottom. The contact is at 22.7 mm (= 6 μs) and gives rise to the prominent reflector marked by arrows.

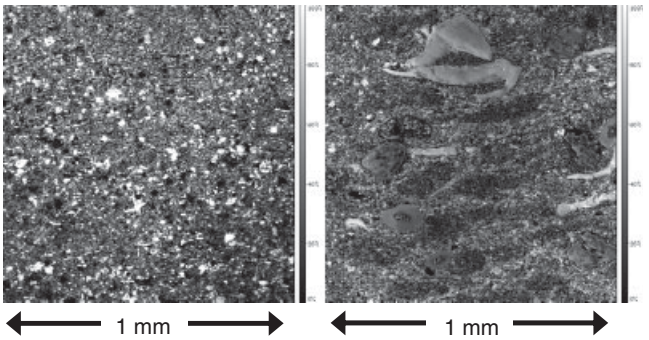

Fig. 4—Acoustic images of an immature Woodford shale (7,068 ft). The two images correspond to the different layers in the sample. One layer (left) has very low impedance and consists of fine-grained, biogenic calcite debris in a matrix of kerogen material and some pyrite. The second layer (right) has aligned lenses of low-impedance material (kerogen + pyrite) alternating with high-impedance, coarser-grained, biogenic (fishbone) calcite debris. The matrix here has intermediate impedance, between the kerogen + pyrite lenses and the organic debris. Note, the gray level in both images has been adjusted to make salient features readily visible.

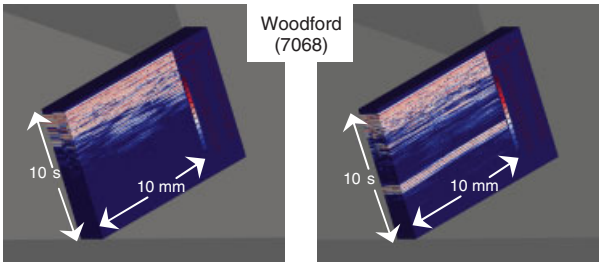

Fig. 5—3D images of the immature Woodford shale (7,068 ft) from Fig. 4. Images from multiple B-scans are combined to trace continuity of reflectors. The two images correspond to the same sample imaged from opposite directions, similar to Fig. 4. In the left image, the coarse-grained, high-impedance layer faces up toward the transducer, and contact between layers is 5.5 mm (= 1.4 μs) below the surface. The acoustic waves first must pass through the coarse-grained layer with the pyrite/kerogen lenses before they hit the boundary. In the right image, the coarse-grained, high-impedance layer is at the bottom and contact between layers is 22.7 mm (= 6 μs) from surface. Despite being farther away from the surface than in the first case, the boundary gives rise to the prominent reflector seen toward the lower half of the image.

show acoustic scans of the Bakken shale at different magnifications, from an expanded view of 62.5 μm (left) to a maximum of 1 mm (right). In Fig. 10, the black colored areas are mostly kerogen material because there is very little porosity in the sample (< 5%). White areas mark grains. The dark colors in the 312-μm image (Fig. 10c) are a result of the acquisition as an impedance calibrated image showing very low impedance in the sample.

From the different-maturity shale samples examined in this study, we find the following major differences in the impedance microstructural images:

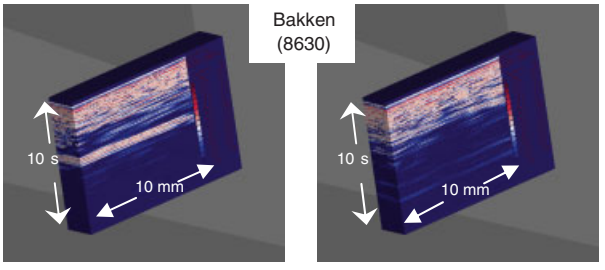

Fig. 6—3D images of the immature Bakken shale (8,630 ft). Images are made from multiple B-scans combined to trace continuity of reflectors. The two images correspond to the same sample imaged from opposite directions: A layer in the top half of the left image is barely visible as discontinuous reflections in the lower part of the right image.

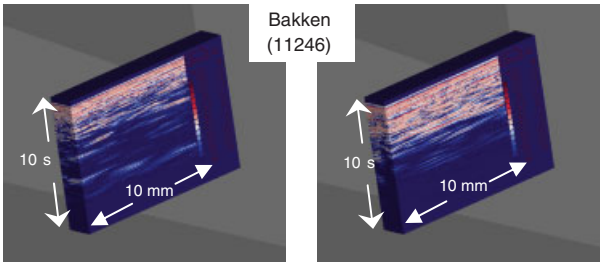

Fig. 7—3D images of the mature Bakken shale (11,246 ft). Images are made from multiple B-scans combined to trace continuity of reflectors. The two images correspond to the same sample imaged from opposite directions. The various reflectors in both images are not continuous over a long distance.

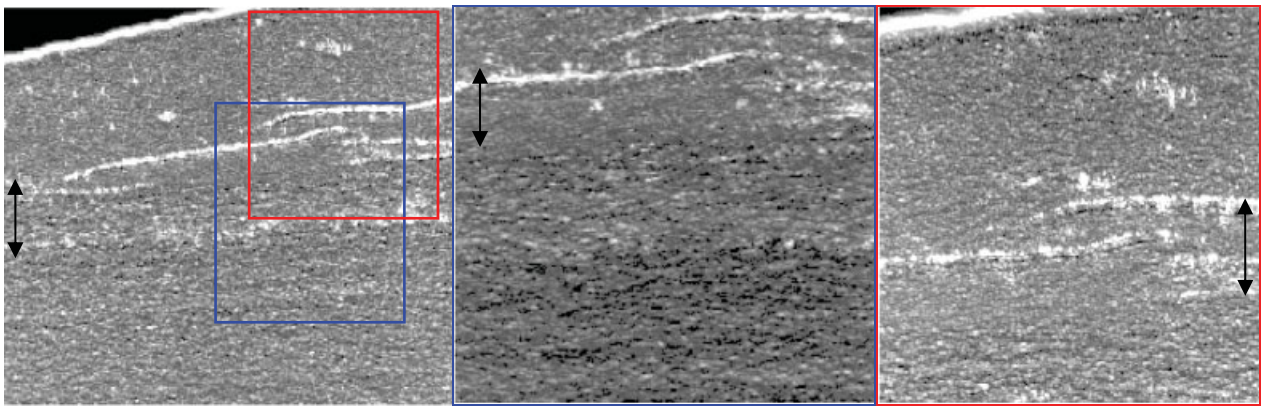

Fig. 8—Acoustic image of a sample from Well Koch 2-28 made at 50 MHz. (a) shows an overview of the sample with the contact zone (marked by arrows) recognized by light bands and lighter grey shades. The image size is 20 × 17.8 mm. (b) A zoomed image of the area shown by the blue box in (a). The image size is 11.8 × 10.8 mm. (c) A zoomed image of the area shown by the red box in (a). The image size is 9.4 × 8.9 mm.

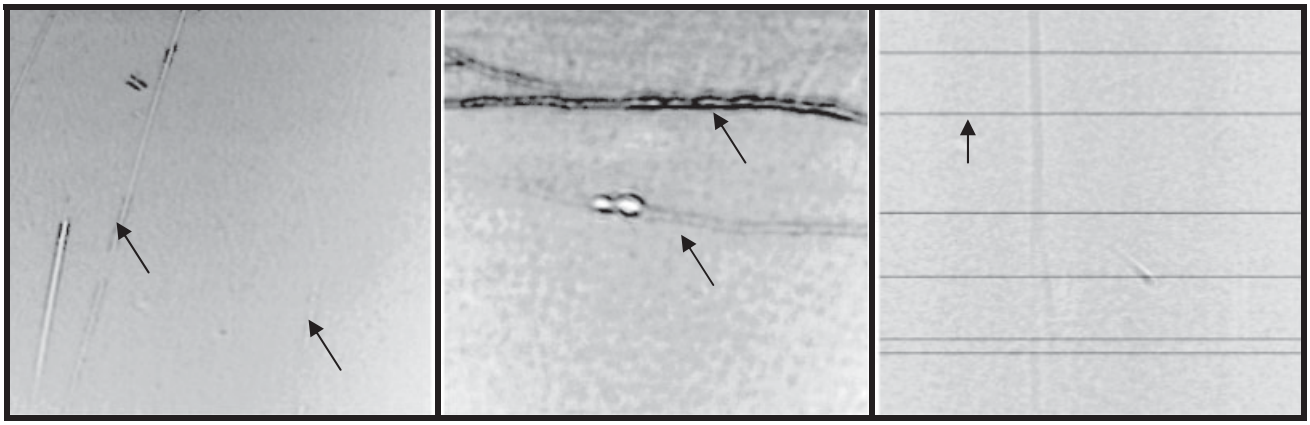

Fig. 9—Acoustic image of samples from Wells HG 21-26H and Koch 2-28 made at 50 MHz. (a) shows the sample HG9052 with some scratches marked by arrows. The image size is 20 × 20 mm. (b) shows the sample HG9056 with horizontal fractures. The image size is 15 × 13.8 mm. (c) shows the sample K7030 with a very uniform texture. Note that the horizontal lines (parallel to the one marked by the arrow) are missing data and do not belong to the texture. The image size is 15 × 40 mm.

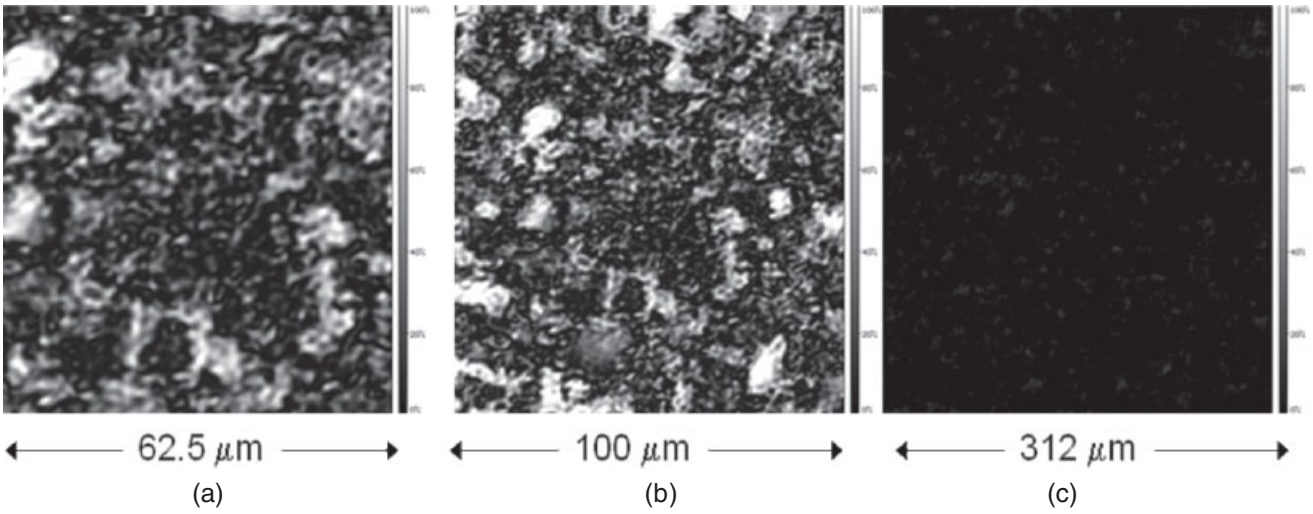

Fig. 10—High-frequency (1-GHz) scan of a low-maturity Bakken shale from the Vernik study. The dark colors imply very low impedance in the sample.

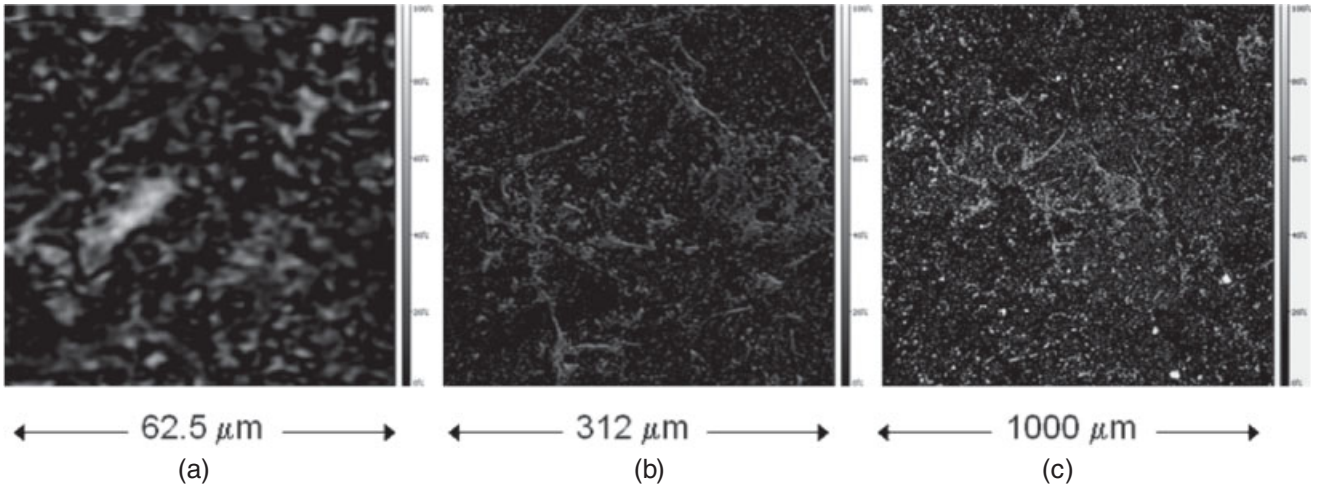

Fig. 11—High-frequency (1-GHz) scan of a medium-maturity Bakken shale from the Vernik study. Note the difference compared with Fig. 10: The grains appear to form bridges (white-colored bands) across the kerogen material.

• Inverse relation between kerogen content, maturity, and impedance

• Increase in grain size and in the number of coarse grains in mature shales

• Major change in kerogen and grain distribution with maturity: In immature shale, kerogen forms a more or less connected matrix and the higher-impedance grains are dispersed in this matrix. In more-mature shale, there is a significant increase in number of coarse grains, and the grains form a framework with kerogen distributed in the pore space.

In the high-frequency images, we assume that all lowest-impedance areas are organic matter. Impedance properties of kerogen are not well known, but we expect it to have the lowest value among all other constituents. Zeszotarski et al. (2004) determined the nanoindentation modulus of kerogen in Woodford shale to be 11 GPa. This modulus value is close to that of a clay/water system (Prasad et al. 2002b). Thus, by mapping the lowest impedance in these clay-poor shales, we expect to map the relative location of the kerogen in the shales.

The microstructure has important applications for mapping the changes in stiffness and impedance of the shales with changing maturity. Lower-maturity organic materials containing a large proportion of aliphatically associated hydrogen tend to have lower density and to deform plastically under load, whereas organic matter with less hydrogen (i.e., higher maturity) has higher density and lower plasticity (Smith and Chong 1984). Thus, the lower-maturity shales with load-bearing organic matter will deform plastically. On the other hand, as the organic matter gets more and more confined to pores, the rock will become stiffer and brittle and could be identified by higher velocities.

Because the amount and location of the organic matter change with maturity, seismic attenuation could be used to map such changes. Internal friction measurements as functions of temperature in coal and ORSs show three peaks corresponding to relaxation mechanisms in the kerogen (Wert and Weller 1982; Weller and Wert 1983). The temperature variation of velocity (either because of maturation in the natural case or because of pyrolysis in the laboratory) could be because of progressive effects with temperature increase of water loss from the shales; pyrolysis of the kerogen; and, finally, cementation of shale matrix by the pyrolysis products (Mraz et al. 1983). This progressive cementation with maturity is also seen in the acoustic images as described in the preceding.

Velocity Analysis. The Vernik data set was analyzed for any correlations between velocity and kerogen content. Such a correlation would help to develop prediction methods using indirect seismic or well-log measurements. **Fig. 13** shows first a density/porosity correlation. The effect of kerogen porosity must be taken into consideration when developing such relations. Similarly, the velocity

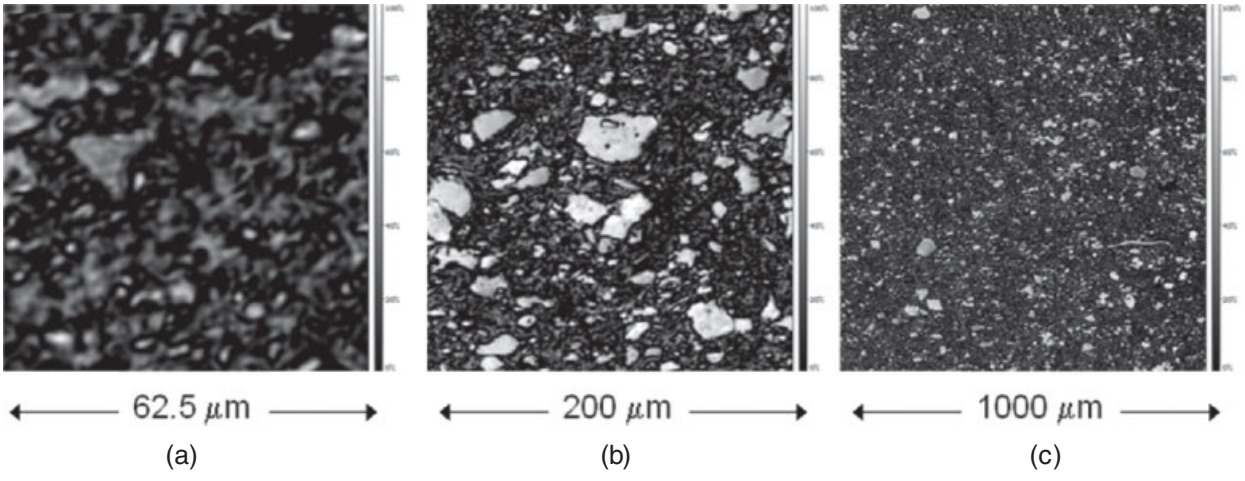

Fig. 12—High-frequency (1-GHz) scan of a high-maturity Bakken shale from the Vernik study. Note the difference compared with Figs. 10 and 11: The texture is much coarser grained (white-colored areas), and the kerogen (black-colored areas) appears in pockets within the grains.

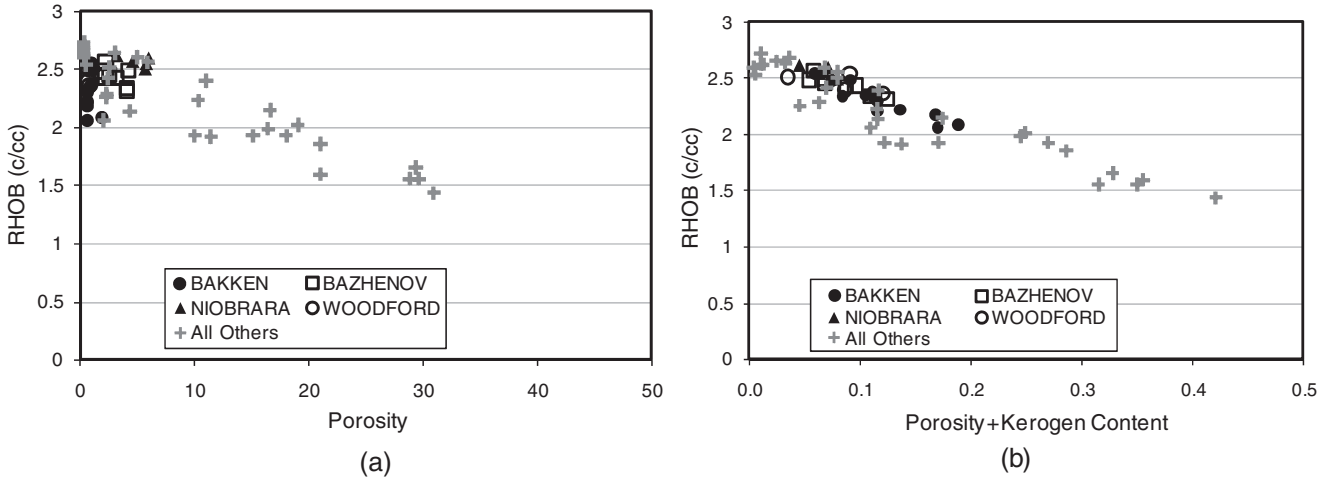

Fig. 13—Bulk density (P_B)/porosity correlation (a) becomes much better if we modify the total porosity by adding the contribution of kerogen content to the porosity (b). In the analysis, we have assumed the kerogen porosity to be 40%. A linear fit through all data in (b) takes the form P_B = –3.1537* modified Kerogen content + 2.6926, with R^2 = 0.84.

relation with porosity or kerogen content is not as good **(Fig. 14).** Within each formation, the velocity/porosity correlation is good, but any general prediction of kerogen content not based on site-specific velocity trends would have large errors.

The scatter in the velocity data in Fig. 14 and the lack of its correlation with porosity and kerogen content could be explained by the fact that although most kerogen shales have low porosity as measured by helium porosimetry, some do have significant pore space. Furthermore, not all of the kerogen is load bearing. Because the presence of both kerogen and porosity leads to velocity reduction, we define a porosity-modified kerogen content by adding total porosity to the kerogen porosity. By trial and error, we determined

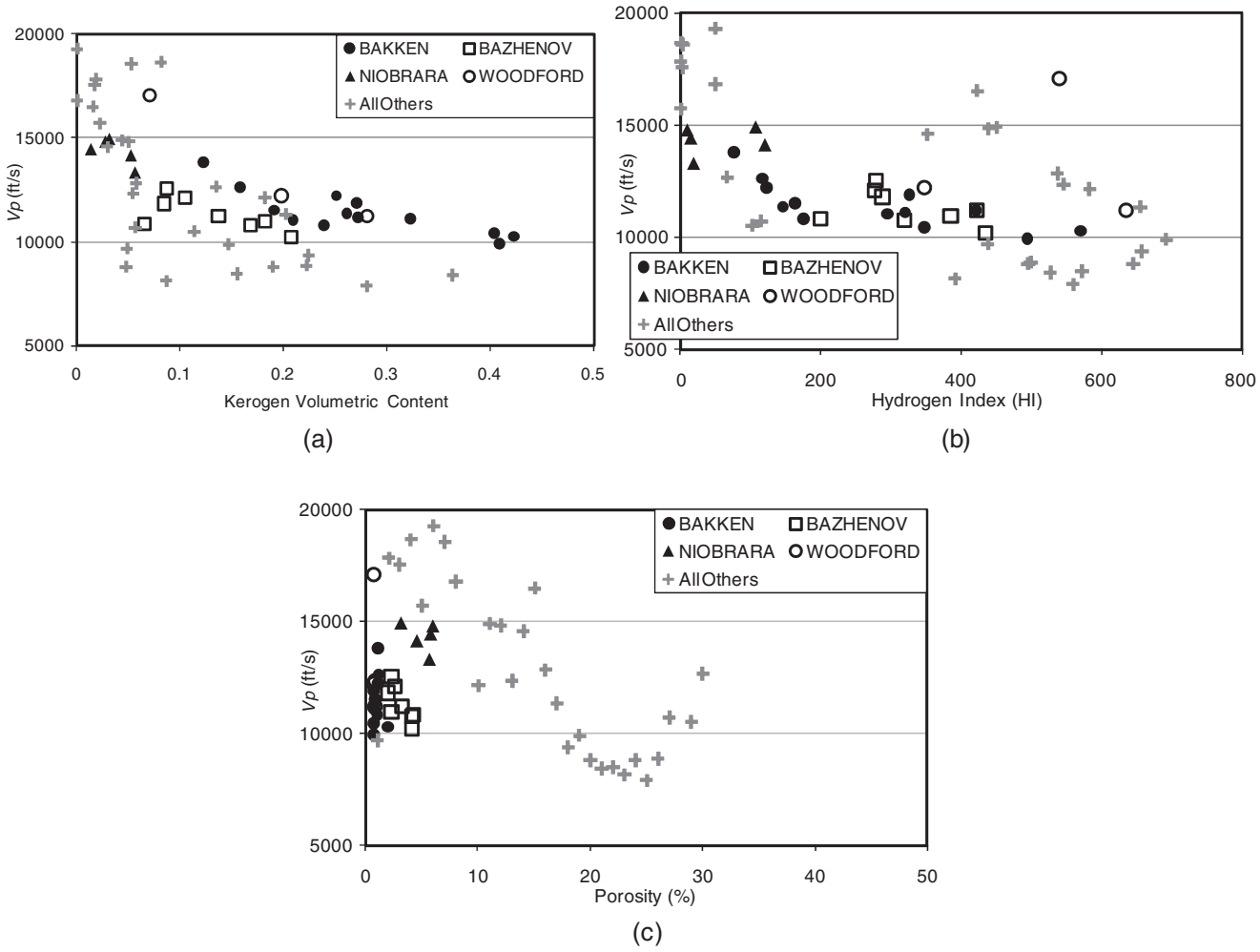

Fig. 14—Horizontal velocity does not correlate very well with kerogen volumetric content (a), with HI (b), and porosity (c). Note that, within any given formation, there is a fairly good correlation.

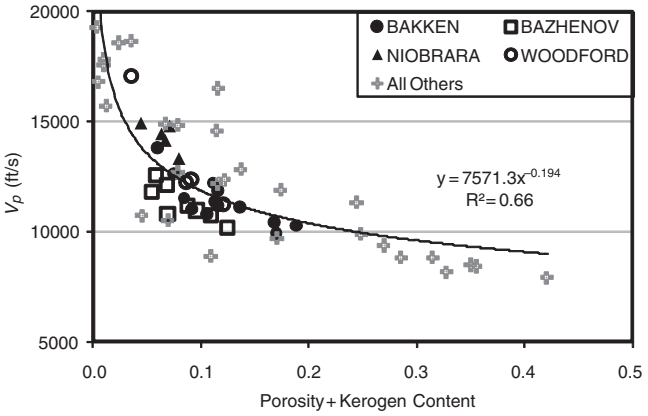

Fig. 15—Horizontal velocity correlates very well with kerogen volumetric content if we assume that approximately 40% of the kerogen acts as pore space to soften the rock. The correlation coefficient between velocity and porosity-modified kerogen content is now significant (R^2 = 0.66) and does not depend on the specific formation.

this porosity to be approximately 40%; this part of the kerogen acts similarly to porosity and further softens the rock. Thus, we add to the total porosity a 40% contribution from kerogen content. Not only is the correlation coefficient now significantly higher, the correlation between velocity and porosity-modified kerogen content is vastly improved and encompasses all formations **(Fig. 15).** The existence of porosity has been demonstrated in scanning-electron-microscope (SEM) images (Loucks et al. 2009; Sondergeld et al. 2010). Our velocity analysis provides a direct consequence of this kerogen porosity: Approximately 40% extra porosity in kerogen is needed to explain modulus variations in different shales from the Vernik data set.

For a number of applications, the anisotropic elastic moduli and stiffnesses of the rocks are needed. We investigated effect of the porosity-modified kerogen content on the anisotropic stiffnesses C11 and C33 shown in **Fig. 16** and C44 and C66 shown in **Fig. 17.** Note that C11 and C33 are derived from V_p measured parallel (V_{p0}) and perpendicular (V_{p90}) to any textural alignments, whereas C44 and C66 are derived from V_s measured parallel (V_{s0}) and perpendicular (V_{s90}) to the textural alignments. The correlation coefficient between the anisotropic moduli and porosity-modified kerogen content is significantly higher than for velocity (R^2 = 0.83 and 0.88 for C11 and C66, respectively, as compared with R^2 = 0.66 for V_p).

Comparison With Log Data. The *P*- and *S*-wave velocities (V_p and V_s, respectively) measured in this study were compared with the Vernik data set and with well logs reported in Meissner (1978). **Fig. 18** shows a comparison of all velocity data. A constant overburden density was assumed in deriving confining pressure for this comparison. Interval transit time, *DT* in Fig. 18a, and V_p in Fig. 18b show similar general trends of increasing velocity with depth. Two outliers plot at just faster than 12,000 ft/sec. The first is from a sample at 7,017 ft with pyrite inclusions, and the other is from the shale sample at the contact with the underlying siltstone formation at a depth of 7,038 ft.

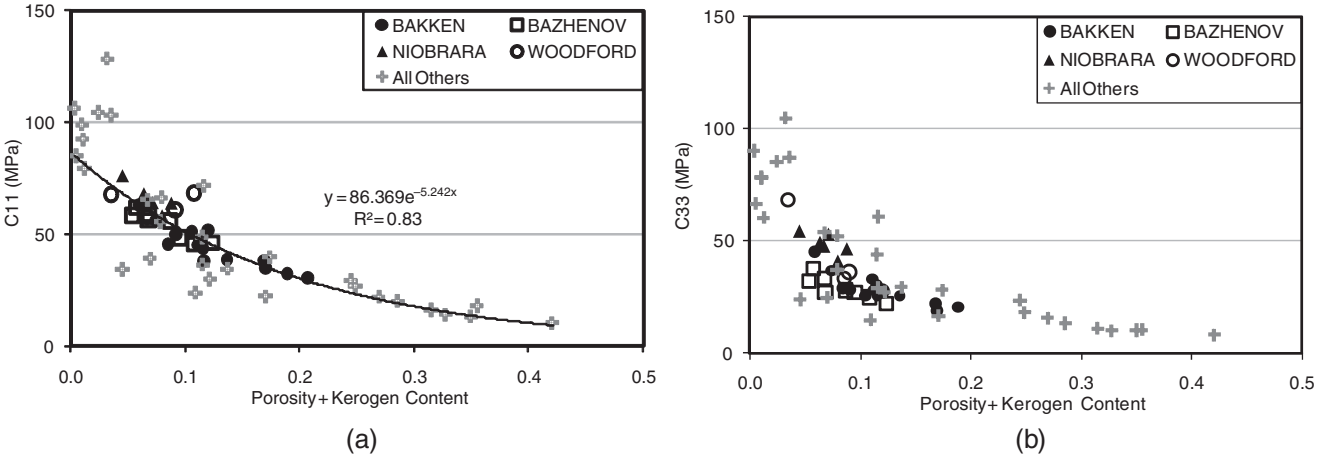

Fig. 16—Elastic moduli [C11 in (a) and C33 in (b)] correlate very well with kerogen volumetric content modified by total porosity.

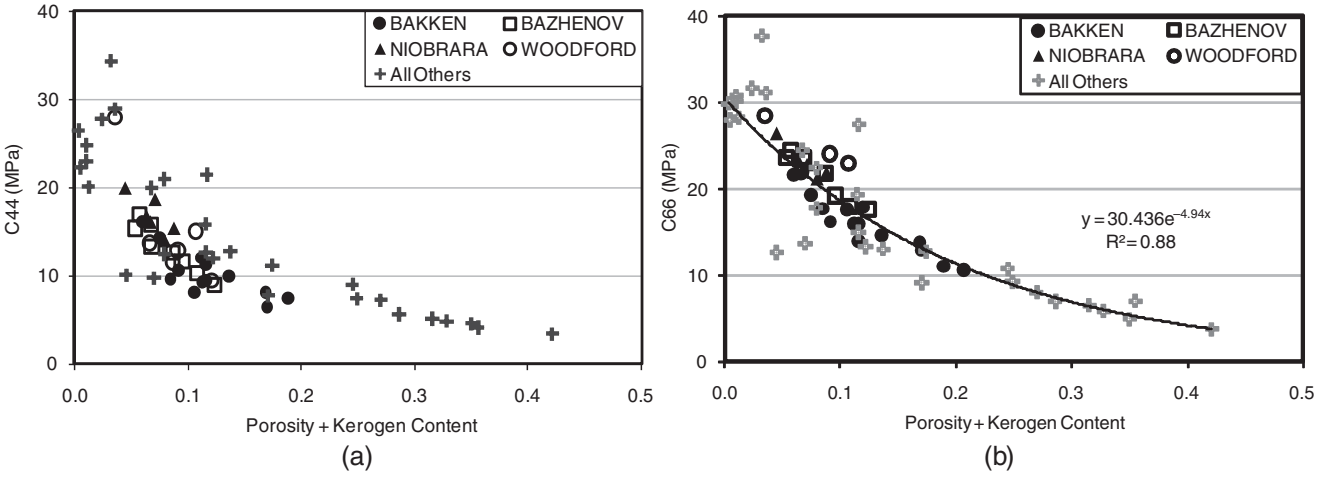

Fig. 17—Elastic moduli [C44 in (a) and C66 in (b)] correlate very well with kerogen volumetric content modified by total porosity.

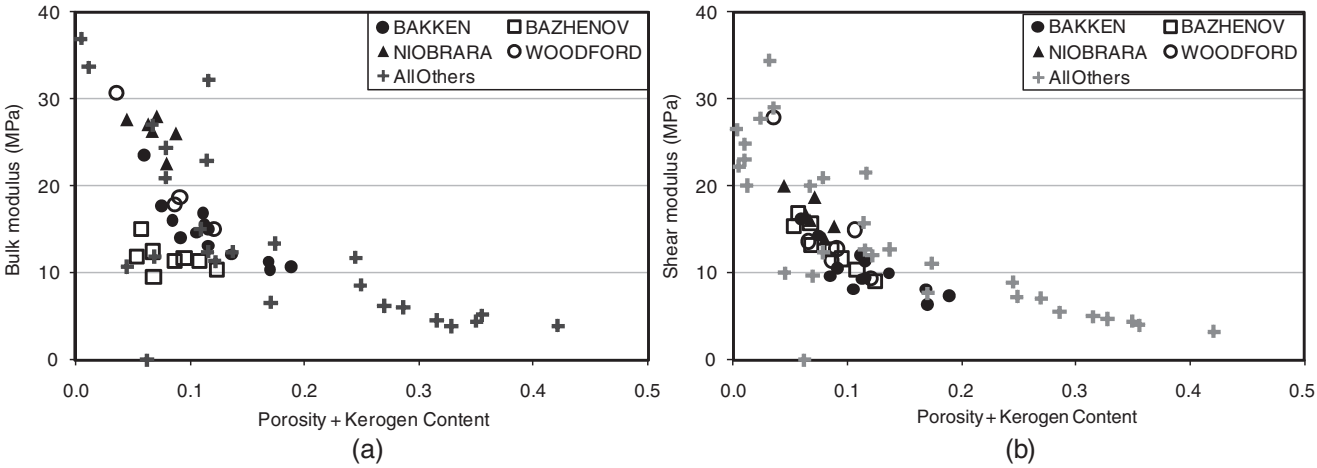

Fig. 18—DT as a function of depth (a) and the same data expressed in V_p as a function of pressure (b). The depth was converted to pressure assuming a constant density in the overburden. Note that the Vernik data (squares) set shows consistently higher velocities than the well-log data (diamonds) from Meissner (1978) and the data collected in this study (triangles). We expect the laboratory data to have a maximum experimental error of 1%.

The difference between laboratory-measured velocities and sonic-log data can lie between 10 and 20%. Fig. 19 illustrates variations between the different measurements. These differences can be because of sample size, frequency of measurements, or core damage because of stress release. For example, sonic logs (red diamonds in Fig. 18) sampled formations at in-situ pressures (Meissner 1978), this study's laboratory values (green triangles in Fig. 19) represent room conditions, and the Vernik velocity data (blue squares in Fig. 18) were measured at a confining pressure of 70 Mpa. The difference between laboratory and log measurements might be mainly because of scaling effects.

1. Formation matrix properties: Laboratory measurements are made on centimeter-sized core plugs; sonic logs are made on meter-sized rock intervals. Thus, the laboratory measurements represent primarily formation matrix properties.

2. Formation bulk properties: Core plugs are often taken at a distance from visible fractures so they are biased toward intact rock. Sonic logs measure the in-situ formation bulk properties.

3. Frequency difference: Laboratory measurements are mostly made in the MHz range. Sonic logs are made at tens of kHz. Laboratory values can be higher than sonic logs because of dispersion effects. However, Jones and Wang (1981) predict a 4% difference in velocities because of dispersion in the Williston basin shales. The data shown here have a larger (more than 10%) difference, reflecting a sampling bias.

Fracture and Strength Considerations for Production Scenarios. Production from the Bakken system is enhanced by an extensive completion and stimulation strategy. Horizontal wells are drilled to encounter a maximum number of natural fractures. Sustained production is maintained through these natural and artificially stimulated fractures. Successful production in unconventional reservoirs is critically dependent on success of the stimulation program. Given their minimal porosity, production mechanisms in ORS formations need an understanding of the fracture mechanism and stress variations.

Experimental studies have shown that static compressive strength is dependent on the kerogen content (Lankford 1976). Similar to the elastic moduli **(Fig. 19),** an increase in TOC tends to decrease compressive strength. With increasing temperatures, higher-TOC shale samples deform predominantly plastically, and pore-pressure buildup leads to tensile microfractures (Lempp et al. 1994). This has important bearing on planning successful production scenarios because hydrofracturing techniques rely on elastic moduli and pore-pressure buildup, and in-situ processing employing some kind of retorting. In order to make reliable estimates of pore-pressure buildup and effective stresses, we calculated Biot's effective stress coefficient using the Vernik data set **(Fig. 20).** Biot's coefficient (α) was calculated from the measured bulk moduli (K) in two directions by assuming a grain modulus (K_s) = 71 GPa (for carbonates) using $\alpha = 1 - (K/K_s)$. This parameter allows us to calculate the effective stress acting on the rock matrix ($P_{\text{eff}} = P_{ob} - \alpha P_p$). Fig. 20 shows that there is a significant deviation in the Biot coefficient from unity. Also, the bulk-modulus anisotropy translates into an anisotropic Biot's coefficient. The Biot's coefficient parallel to bedding is lower than that perpendicular to bedding.

We used the dynamic bulk modulus at elevated pressures (70 MPa) to calculate Biot's coefficient. Although a certain amount of dispersion exists between the dynamic and static moduli, the two approach each other at the elevated pressure of 70 MPa used here. The reasons for the anisotropy are set forth in Prasad et al. (2009). Suffice it to say that alignments of clay and kerogen layers are the most likely candidates to explain the velocity differences.

A few key observations critical to future planning can be made from Fig. 20:

1. The Biot's coefficient is less than unity and is inversely proportional to maturity, decreasing to below 0.6 for mature ORSs. Any in-situ pyrolysis to generate pore pressures as well as hydraulic-fracture stimulations will need to take these low Biot coefficients into consideration. Furthermore, the stimulation scheme would also need to be adapted to the maturity level of the formation.

2. The magnitude of anisotropy in Biot coefficient is high, and it remains constant regardless of kerogen content. In Fig. 20, open circles are values derived from measurements perpendicular to bedding (slow direction) while solid circles are derived from measurements parallel to bedding (fast direction). In continuation of Point 1, the stimulation planning will need to address the prevalent formation anisotropy.

3. The Bakken formation is known to have significantly high pore-pressure gradient in some parts of the depositional basin (Cramer 1986).

Conclusions

1. The correlation between kerogen content and elastic properties is significantly better if we use porosity-modified kerogen content and assume a kerogen porosity equal to 40%.
2. There is an inverse correlation between stiffness and modified-porosity kerogen content. For example, the C66 stiffness can be predicted by $C66 = 30.436e^{-4.94*\text{modified kerogen}}$, with an $R^2 = 0.88$.
3. There is an increase in grain size and in the number of coarse grains in mature shales.

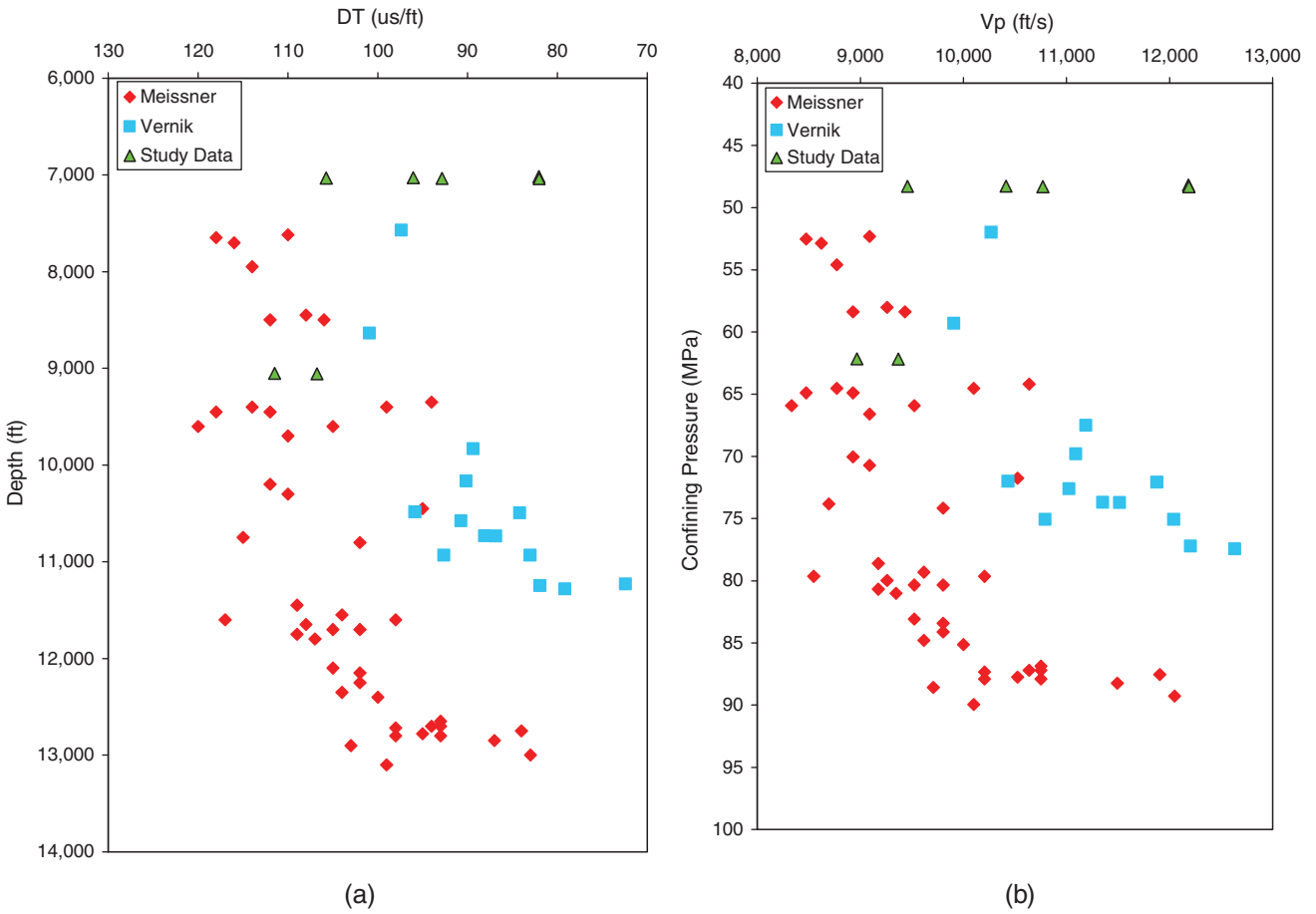

Fig. 19—Bulk (a) and shear (b) moduli as functions of the modified porosity. As in the stiffnesses, there is a significant inverse correlation of the moduli with the porosity-modified kerogen content.

4. There is a major change in kerogen and grain distribution with maturity: In immature shale, kerogen forms a more or less connected matrix and the higher-impedance grains are dispersed in this matrix. In more-mature shale, there is a significant increase in the number of coarse grains and the grains form a framework with kerogen distributed in the pore space.
5. The Biot's coefficient is less than unity and is inversely proportional to maturity, decreasing to below 0.6 for mature ORSs.

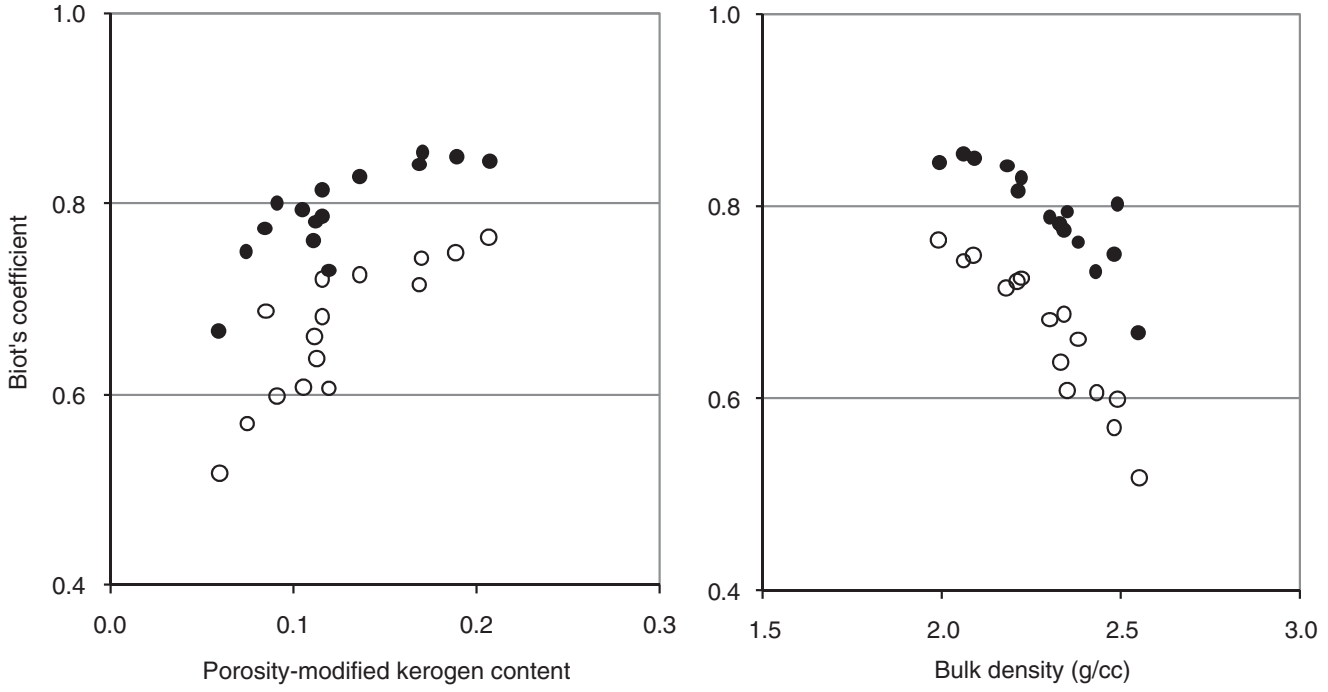

Fig. 20—Bedding-parallel (open circles) and bedding-perpendicular (solid circles) Biot's coefficient calculated from the Vernik data set as function of porosity-modified kerogen content (a) and bulk density (b).

Ultrasonic imagery using scanning acoustic microscopy was successful in characterizing the kerogen content and maturity of ORSs. Integration of impedance data from these measurements with observations from optical microscopy and downhole sonic data can lead to useful correlations for detecting shale maturity through indirect surface measurements. In this study, relationships have been established between velocity and porosity and between velocity and kerogen content. Future formation-specific evaluation work is planned for integration of the evolution of microfractures during the course of maturation with microstructural texture variation, kerogen content, and shale maturity.

Acknowledgments

We thank Lev Vernik for his suggestion to investigate ORSs and his valuable input. This work was supported by a grant from DOE (Award#: DE-NT0005672) and by the Direct Hydrocarbon Indicator/Fluids consortium at the Colorado School of Mines. The GHz-range and some MHz-range images were made using the acoustic microscope facilities of the Fraunhofer Institute for Nondestructive Test Methods (IzfP) in Germany for the-acoustic microscope studies. Manika Prasad thanks the IzfP and Walter Arnold for allowing use of their facilities so freely and Krämer Scientific Instruments for a grant toward the SAM.

References

Briggs, A. and Kolosov, O. 1992. *Acoustic Microscopy*, 47. Oxford, UK: Monographs on the Physics and Chemistry of Materials, Oxford University Press.

Cramer, D.D. 1986. Reservoir Characteristics and Stimulation Techniques in the Bakken Formation and Adjacent Beds, Billings Nose Area, Williston Basin. Paper SPE 15166 presented at the SPE Rocky Mountain Regional Meeting, Billings, Montana, USA, 19–21 May. http://dx.doi.org/10.2118/15166-MS.

Jones, L.E.A. and Wang, H.F. 1981. Ultrasonic velocities in Cretaceous shales from the Williston Basin. *Geophysics* **46** (3): 288–297. http://dx.doi.org/10.1190/1.1441199.

Lankford, J. Jr. 1976. Dynamic Strength of Oil Shale. *SPE J.* **16** (1): 17–22. SPE-5327-PA. http://dx.doi.org/10.2118/5327-PA.

Lempp, C., Natau, O., Bayer, U., and Welte, D.H. 1994. The effect of temperature on rock mechanical properties and fracture mechanisms in source rocks - Experimental results. Paper SPE 28039 presented at the Rock Mechanics in Petroleum Engineering, Delft, The Netherlands, 29–31 August. http://dx.doi.org/10.2118/28039-MS.

Lewan, M.D. 1987. Petrographic study of primary petroleum migration in the Woodford Shale and related rock units. In *Migration of Hydrocarbons in Sedimentary Basins*, ed. B. Doligez, No. 45, 113–130. Paris: IFP ERC Proceedings, Editions Technip.

Loucks, R.G., Reed, R.M., Ruppel, S.C., and Jarvie, D.M. 2009. Morphology, Genesis, and Distribution of Nanometer-Scale Pores in Siliceous Mudstones of the Mississippian Barnett Shale. *J. Sediment. Res.* **79** (12): 848–861. http://dx.doi.org/10.2110/jsr.2009.092.

Meissner, F.F. 1978. Petroleum geology of the Bakken Formation, Williston basin, North Dakota and Montana. In *The Economic Geology of the Williston Basin: Proceedings of the Montana Geological Society, 24th Annual Conference*, ed. D. Rehrig, 207–227. Billings, Montana: Montana Geological Society.

Mraz, T., DuBow, J., and Rajeshwar, K. 1983. Acoustic wave propagation in oil shale: 1. Experiments. *Fuel* **62** (10): 1215–1222. http://dx.doi.org/10.1016/0016-2361(83)90066-2.

Passey, Q.R., Creaney, S., Kulla, J.B., Moretti, F.J., and Stroud, J.D. 1990. A practical model for organic richness from porosity and resistivity logs. *AAPG Bull.* **74** (12): 1777–1794.

Prasad, M. 2001. Mapping impedance microstructures in rocks with acoustic microscopy. *The Leading Edge* **20** (2): 172–179. http://dx.doi.org/10.1190/1.1438902.

Prasad, M., Reinstädler, M., Nur, A., and Arnold, W. 2002a. Quantitative Acoustic Microscopy: Application to Petrophysical Studies of Reservoir Rocks. In *Acoustical Imaging*, ed. R.G. Maev, Vol. 26, Part 8, 381–387. New York: Kluwer Academic/Plenum Publishers.

Prasad, M., Kopycinska, M., Rabe, U., and Arnold, W. 2002b. Measurement of Young's modulus of clay minerals using atomic force acoustic microscopy. *Geophys. Res. Lett.* **29** (8): 1172. http://dx.doi.org/10.1029/2001gl014054.

Prasad, M., Mukerji, T., Reinstaedler, M., and Arnold, W. 2009. Acoustic Signatures, Impedance Microstructure, Textural Scales, and Anisotropy of Kerogen-Rich Shales. Paper SPE 124840 presented at the SPE Annual Technical Conference and Exhibition, New Orleans, 4–7 October. http://dx.doi.org/10.2118/124840-MS.

Smith, J.W. and Chong, K.P. ed. 1984. *Mechanics of Oil Shale*. London: Elsevier Applied Science Publishers.

Sondergeld, C.H., Ambrose, R.J., Rai, C.S., and Moncrieff, J. 2010. Micro-Structural Studies of Gas Shales. Paper SPE 131771 presented at the SPE Unconventional Gas Conference, Pittsburg, Pennsylvania, USA, 23–25 February. http://dx.doi.org/10.2118/131771-MS.

Vernik, L. and Landis, C. 1996. Elastic anisotropy of source rocks; implications for hydrocarbon generation and primary migration. *AAPG Bull.* **80** (4): 531–544.

Vernik, L. and Liu, X. 1997. Velocity anisotropy in shales: A petrophysical study. *Geophysics* **62** (2): 521–532. http://dx.doi.org/10.1190/1.1444162.

Vernik, L. and Nur, A. 1992. Ultrasonic velocity and anisotropy of hydrocarbon source rocks. *Geophysics* **57** (5): 727–735. http://dx.doi.org/10.1190/1.1443286.

Weller, M. and Wert, C.A. 1983. Internal friction of coals and of other natural macromolecular solids. *Journal de Physique* **44** (12): Colloque C9, 191–196.

Wert, C.A. and Weller, M. 1982. Polymeric character of coal. *J. Appl. Phys.* **53** (10): 6505–6512. http://dx.doi.org/10.1063/1.330076.

Zeszotarski, J.C., Chromik, R.R., Vinci, R.P., Messmer, M.C., Michels, R., and Larsen, J.W. 2004. Imaging and mechanical property measurements of kerogen via nanoindentation. *Geochim. Cosmochim. Acta* **68** (20): 4113–4119. http://dx.doi.org/10.1016/j.gca.2003.11.031.

Manika Prasad is an associate professor in petroleum engineering at the Colorado School of Mines. Her main interests lie in rock physics and in understanding what is unconventional about shales. **Tracy McEvoy** is a graduate of the geophysical engineering department at the Colorado School of Mines. **Michael Batzle** is co-director of the Center for Rock abuse and a professor in the geophysics department at the Colorado School of Mines. **Kenechukwu C. Mba** works for ExxonMobil in Nigeria. Kene holds a BS degree in geology and an MS degree in petroleum engineering.